



Velocity measurements in particle-laden high-enthalpy flow using non-intrusive techniques

Ciro Salvi¹ · Ali Gülhan¹

Received: 5 December 2023 / Revised: 26 January 2024 / Accepted: 30 January 2024 / Published online: 6 March 2024
© The Author(s) 2024

Abstract

This research aims at analysing the particle-laden flow of the hypersonic high-enthalpy wind tunnel L2K, situated in Köln at the German Aerospace Center (DLR). In the L2K wind tunnel, Martian atmosphere can be created, and the facility can simulate heat load conditions encountered during atmospheric entry of Martian missions. In the tests, a simplified Martian atmosphere (97% CO₂ and 3% N₂) was used. The high-enthalpy flow was loaded with micrometric particles of magnesium oxide. The particles' mean velocity was measured with a 2D–2C particle image velocimetry (PIV) system, in the region right downstream the nozzle expansion of the wind tunnel. The work proves the possibility of creating a high-enthalpy particle-laden flow for thermal protection systems (TPS) testing with simulated Martian atmosphere. Average particle velocities of around 2000 m/s are measured and compared with the numerical simulation of the wind tunnel's particle-free flow, and with the flow velocity measured with tunable diode laser absorption spectroscopy (TDLAS). The study also highlights some unexpected results and features of the high-enthalpy particle-laden flow and proposes some theories for the causes of such effects, which include agglomeration due to melting, and gravitational effect.

1 Introduction

Spacecraft design for missions to Mars requires resistance to encountered heat loads during atmospheric entry, which is a manoeuvre in hypersonic regime characterized by high temperature effects. External thermal protection systems (TPS) are needed in this phase to grant spacecraft survivability. In addition to high temperature effects, the presence of dust particles in the Martian atmosphere needs to be considered, as mentioned in Palmer et al. (2020), since particles concentration can vary according to Martian weather: several major dust storms were observed in the past years, where dust presence could extend up to altitudes of 80 km. It was experimentally proven in Keller et al. (2010) that the presence of particles suspension during atmospheric entry enhances the heat loads on spacecrafts' TPS. On-ground simulations of dust-laden flows encountered in Martian atmospheric entry

are necessary for the optimization of spacecraft heat shields, aimed at increasing reliability, reducing mass, thus reducing overall mission costs. Experimental characterization of TPS materials requires an upgrade of the operation mode and measurement techniques of existing long duration high-enthalpy facilities.

Significant uncertainty still exists on particle-enhanced heat flux, both in terms of mathematical modelling and in numerical rebuilding. Experimental campaigns in long duration high-enthalpy facilities can give multiple benefits, such as bringing physical insight into the complex phenomena happening in these high-temperature regimes, and providing validation tools for the existing—or newly developed—numerical models.

For these reasons, recent years were characterized by the renewed scientific interest towards particle-laden flows (Palmer et al. 2022), for which a cooperation between NASA Ames research center and the German Aerospace Center (DLR) was established, aiming at delving deeply into dusty flow modelling and simulation, supported by experimental campaigns. Supersonic particle-laden flows were comprehensively analysed in Allofs et al. (2022), where simultaneous determination of particle size, velocity, and mass flow, was performed by means of Particle Tracking Velocimetry (PTV) and shadowgraphy.

✉ Ciro Salvi
ciro.salvi@dlr.de
Ali Gülhan
ali.guelhan@dlr.de

¹ Supersonic and Hypersonic Technologies Department, German Aerospace Center (DLR), Linder Höhe, 51147 Köln, Germany

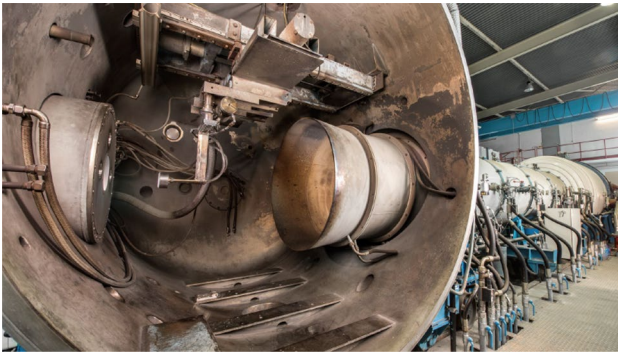


Fig. 1 The L2K high-enthalpy wind tunnel test section

Feasibility of such experimental techniques was thus confirmed in the GBK wind tunnel (multiple phase flow facility), of the *Supersonic and Hypersonic Technologies Department* at DLR Köln. GBK is a small wind tunnel where the flow can be heated up to 800 K, allowing easy optical access and operations. Building up on this knowledge, experimental studies in the L2K wind tunnel at DLR Köln (arc-heated wind tunnel, Fig. 1) should be performed, to include high-enthalpy effects, thus increasing the accuracy of Martian atmospheric entry simulation. L2K wind tunnel is described in Sect. 2 (as in Salvi et al. 2023).

Particle imaging-based techniques need to be implemented in the wind tunnel for the characterization of the particle-laden flow: particle image velocimetry (PIV) was implemented in this work with the goal of measuring particles' mean velocity in the free stream, obtaining a first important result for understanding particles' behaviour in the high-enthalpy wind tunnel, as a first step towards future experiments for TPS characterization. PIV is a widely established experimental technique comprehensively described in Raffel et al. (2018), which spreads across the most diverse fields of flow imaging. It was implemented in hypersonic wind tunnels, such as in blow-down wind tunnels (Neeb et al. 2018; Lu et al. 2019; Schrijer et al. 2006) and in shock tubes (Kirmse et al. 2011; Gnemmi et al. 2010). In Gnemmi et al. (2010), particle speeds of about 2500 m/s were measured, confirming that with proper hardware settings, hypervelocities can be measured. PIV was applied in an arc-heated facility for supersonic combustion testing, where specific enthalpy of 3.5 MJ/kg were measured (Sub Lee et al. 2022).

PIV applied to a long duration arc-heated wind tunnel dedicated to thermal protection systems (TPS) testing was never performed. In such a facility, the flow's low density, combined with the high temperatures of the reservoir, make particle seeding and particle imaging techniques quite

challenging. Particle-laden flows in L2K were studied in Keller et al. (2010) and in MDUST (2006), where Laser-to-Focus (L2F) technique was applied. Differently from L2F, PIV allows velocity measurement on a broad region of interest, though being more limited on the resolution, by the used camera objective.

This work presents the implementation of 2D–2C PIV in the L2K arc-heated wind tunnel. Particles' velocities of more than 2 km/s were measured. The computed results highlighted peculiar phenomena, such as agglomeration due to melting and the importance of gravity, later discussed. The results are then compared with non-equilibrium CFD simulations of the free-stream without particles, and with tunable diode laser absorption spectroscopy (TDLAS) measurements on flow axis, performed in Salvi et al. (2023). In the following sections, the arc-heated facility L2K and the experimental setup will be presented; then, experimental results will be reported and discussed; in the end, conclusions and outlook will be given.

2 Arc-heated facility L2K

As reported in Salvi et al. (2023), L2K is an arc-heated continuous-flow high-enthalpy wind tunnel suited for TPS materials testing and components' demisability tests, as it can provide high heat fluxes for long testing times, at the expense of aerodynamic properties characterization: the low density environment causes Reynolds number to be too low compared to atmospheric entry. In such conditions it is important to consider a reacting non-equilibrium flow. L2K reservoir is energized by a 1.4 MW Huels-type arc heater which grants the flow a high specific enthalpy thanks to the electrical discharge. Flow conditions can be varied with different degrees of freedom, such as mass flow rate, reservoir pressure, nozzle exit diameter, sample position, and chamber background pressure, which grant a wide range of operating conditions of the testing facility. Heat flux varies also on flow axis, thanks to the nozzle's geometry, that causes flow post-expansion. A broad selection of intrusive and non-intrusive measurement techniques can be used (for instance, thermocouples, thermocameras, pyrometers, Pitot probes, tunable diode laser absorption spectroscopy or TDLAS, laser-induced fluorescence or LIF, Fourier transform infrared spectroscopy or FTIR).

The analysed flow conditions (FC) were defined by DLR in the post-flight analysis of ESA ExoMars 2016 mission (ESA. ExoMars 2022) and are reported in Table 1, from Salvi et al. (2023). L2K nozzle geometry to be used is reported in Fig. 2.

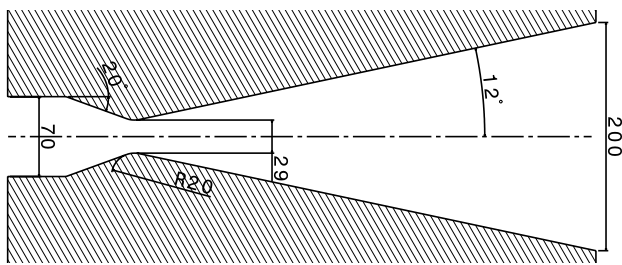


Fig. 2 L2K nozzle geometry, 200 mm exit diameter configuration. Sizes in mm

Table 1 Flow conditions

Parameter	FCI	FCII
Total mass flow rate, [g/s]	41.2	
Mass flow rate CO ₂ (97%), [g/s]	40	
Mass flow rate N ₂ (3%), [g/s]	1.2	
Reservoir pressure, [hPa]	790	930
Predicted specific enthalpy*, [MJ/kg]	5.6	9.2
Predicted reservoir temperature*, [K]	2815	3283

*Estimated with quasi-1D flow solver NATA, as in Salvi et al. (2023)

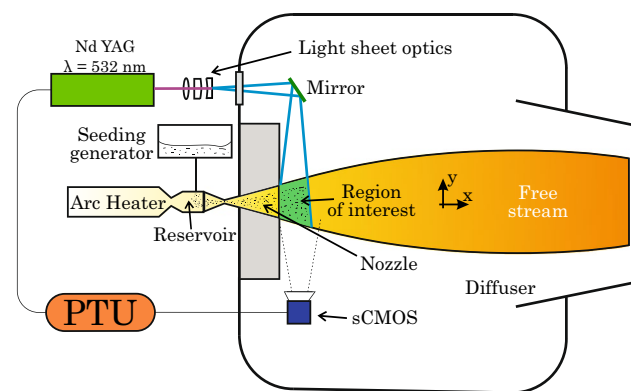


Fig. 3 Experimental setup sketch. The reported axes originate on flow axes, at the nozzle exit location

3 Experimental setup

Particle image velocimetry (PIV)

A 2D–2C PIV setup was implemented as sketched in Fig. 3. The coordinate system is defined as follows: the x -axis coincides with the nozzle symmetry axis, it originates at the nozzle exit, and x values are positive downstream (towards right, referring to the picture); the y -axis defines the transversal direction, it originates on flow axis, and y values increment towards the top of the wind tunnel;

both axes belong to the laser sheet plane. A seeding generator inserts particles in the L2K flow before nozzle expansion. A programmable timing unit (PTU) synchronizes the laser that illuminates particles in the region of interest, and the camera that takes two pictures at a defined time distance of the particles. The time interval Δt is referred as interframing time,¹ and it is the time distance between two laser pulses. The process can be repeated with a repetition rate dependent on hardware characteristics. The two subsequent PIV images are then processed with cross-correlation algorithms to obtain an average velocity of the selected Interrogation Windows (IW, i.e. the pixels of the PIV result). A comprehensive description of PIV experimental technique can be found in Raffel et al. (2018).

One dual-cavity Nd-YAG laser (Quantel Big Sky) was used as light source, with 15 Hz repetition rate. The selected interframing time is $\Delta t = 1 \mu\text{s}$. The time difference between two adjacent laser pulses was monitored with an oscilloscope, that highlighted high time stability and a variation of less than 0.1%: the average measured time difference between two pulses is $(1000 \pm 0.5) \text{ ns}$. The light beam was focused on flow axis and transformed into a light sheet with a cylindrical lens ($f = -50 \text{ mm}$). The light sheet crosses L2K flow vertically, with the nozzle axis belonging to the light sheet plane, and its thickness is approximately 1 mm. The light sheet illuminates the region downstream of the nozzle exit, from the nozzle exit to—at least—80 mm downstream.

One LaVision imager sCMOS camera was used. Between the sensor and the objective, a narrowband filter was positioned, with FWHM = 2 nm around 532 nm. The imager observes the light sheet plane perpendicularly (note that in Fig. 3 the imager is represented on a wrong plane for schematic visualization purposes only; same for the particles injection, which happens on the horizontal mid-plane of the settling chamber). The imager has a $6.5 \mu\text{m}$ pixel size, and a $2560 \times 2160 \text{ px}^2$ maximum resolution. The minimum achievable interframing time is 120 ns.

The “short side” of the camera (2160 px) was positioned parallel to the nozzle axis, to picture the widest illuminated region. With a 50 mm objective, the “long side” of the camera can picture the whole nozzle exit diameter, so to visualize the whole flowfield at the exit of the nozzle. In particular, the “long side” pictures 210 mm: the image resolution is 12.2 px/mm for such objective. The short side thus pictures 177 mm: part of the image will not be used in PIV evaluation, as the light sheet is only approximately 80 mm large. Expecting particle speed of about 2 km/s (from Salvi et al. 2023), and with the chosen

¹ The interframing time is—in these hypersonic conditions—too short to take more than two subsequent pictures, with the used hardware.

Table 2 Test matrix

Test n.	Objective	FC	N. Images
1	2.8/50 mm	I	1350
		II	1500
2	2/100 mm	I, II	2000

interframing time of 1 μ s, the expected displacement of the particles between two frames is 2 mm, corresponding to approximately 24 px. With a similar camera orientation, and a 100 mm objective, the camera pictures $90 \times 75 \text{ mm}^2$, granting a resolution of 28.5 px/mm, and an expected particle displacement of 57 px with the selected interframing time. Due to the large expected particle displacement, and thanks to the uniformity of the expected particles velocity field, a multi-pass PIV algorithm with window shift was used for processing.

The seeding generator is a pressurized vessel working with a bypass flow of 2 g/s, taken from the main CO_2 flow: to keep the mass flow rate as specified in Table 1, 38 g/s of CO_2 are heated in the arc-heater together with 1.2 g/s of N_2 , while 2 g/s of CO_2 are used for collecting the particles inside the pressurized vessel. The cold bypass flow is re-inserted into the main—already heated—flow, right before the nozzle expansion. The injection of the bypass flow into the wind tunnel's reservoir happens on the horizontal plane. Particles of magnesium oxide (MgO) are stored inside the pressurized vessel. The used particles are LUVOMAG[®] M SF, 95 % of which range between 1 μ m and 3 μ m, as specified by the producer.

Testing times are limited by the amount of particles stored in the seeding generator before testing. The results of two test campaigns—whose main parameters are summarized in Table 2—are reported in this work. During the first campaign, 1350 double-frame PIV images were taken for FCI, and 1500 for FCII, with testing times of approximately 90 s. A 2.8/50 mm objective was used for the sCMOS camera. In the second campaign a different objective was used (2/100 mm) to observe a zoomed region on flow axis and increase spatial resolution. For the second test campaign, 2000 pictures were taken for both FCs, with testing times of approximately two minutes.

In the following section, results are reported.

Tunable diode laser absorption spectroscopy (TDLAS)

TDLAS technique consists in using a narrow band diode laser whose peak can be shifted in wavelength, up to few nm; this feature can be used to scan narrow spectra, around a central wavelength where an absorption line is expected. TDLAS was used for flow analysis, as it is a line-of-sight non-intrusive technique that permits to measure flow speed and observed species' concentration on defined measurement

lines. The velocity of the flow core can be inferred by a profile-fitting approach. In the following, the term “point measurement” will refer to the result of the flow core velocity value, obtained with the mentioned approach, which is reported in detail in Salvi et al. (2023). The TDLAS analysis reported in Salvi et al. (2023) is cited here for comparison purposes with PIV data: while PIV evaluates the particles' velocities, TDLAS measures the flow speed on flow axis. By comparing the results obtained with the two experimental techniques, one can have a hint on the velocity lag between particles and flow. TDLAS flow diagnostic was performed without particles, measuring velocities in three points on flow axis, corresponding to $x = \{100, 200, 300\}$ mm downstream nozzle exit, at the same two flow conditions mentioned in Table 1. Figure 3 in Salvi et al. (2023) shows the conceptual scheme of the experimental setup, and Figure 26 of the same paper reports the measured flow velocity. In this work, only the point-measurement relative to $x = 100$ mm is highlighted, in the next section.

4 Results

In this section, general observation on the PIV experimental campaigns in L2K is reported, and then, results are presented and discussed in detail.

4.1 General considerations

As this is the first paper reporting PIV in an arc-heated wind tunnel for TPS testing, it is worth spending some lines on general considerations and data quality. Contrarily to some experimental activities in other hypersonic wind tunnels, the depressurization process of the test chamber did not affect laser line's stability and alignment, making the calibration process relatively simple, thanks to the massive structure of the L2K facility and its relatively low mass flow rates. Also, the camera's focus was not affected by the chamber depressurization, and no vibrations were observed. The injection of particles inside the hot reservoir did not cause any flow instability. Particles seeding was granted for up to two minutes, and seeding quality varied with time: some pictures have perfect homogeneous seeding, some have only a region with good seeding, and some counted only few particles. For this reason, the correct choice of vector validation and filtering technique is crucial in data processing, and it is reported in Sect. 4.2.

Another issue is the formation of agglomerates: the high temperature of the reservoir can cause the particles to melt, and stick together after colliding. The agglomeration process is uncontrollable, and it can be mild (if only few micrometric particles agglomerate) or severe, if the agglomerate is big enough to keep glowing while travelling through the nozzle and test chamber: in this case the cooling time of

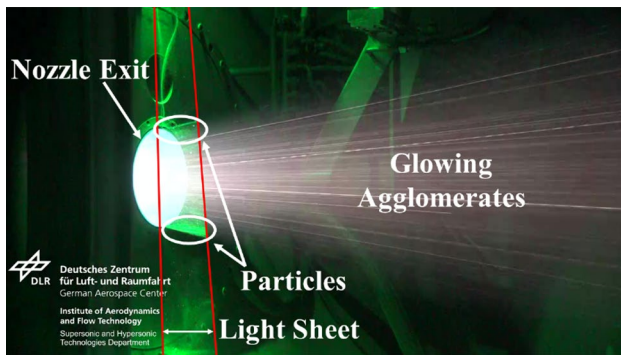


Fig. 4 Wind tunnel test frame from the video monitoring

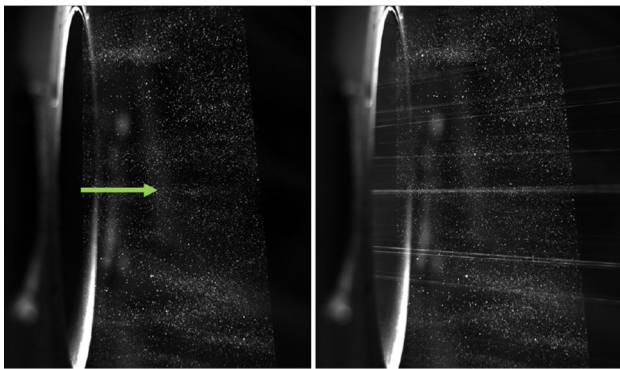


Fig. 5 Generic PIV raw image, first frame (left) and second frame (right). The green vector represents nozzle axis and flow direction

the agglomerate is longer than the time that the agglomerate takes to travel through the test chamber. The glowing agglomerates can be observed in the frames of the video monitoring of the wind tunnel tests (Fig. 4), as well as the second frame of the PIV acquisition (Fig. 5, right), as they are characterized by long exposure times: the glowing agglomerates appear as bright stripes in such frames. The presence of glowing agglomerates was observed even after the shutdown of the seeding generator. The glowing agglomerates cannot be used for PIV evaluations. They also affect data quality, since they can easily reach the same intensity of isolated particles. Agglomerates' brightness cannot be reduced in the pictures, but particles' signal can be increased, by increasing laser output power, and by using a different cylindrical lens (thus reducing the angular expansion of the light sheet). Differently from particles, which are visible thanks to laser light scattering—making them seen only on the light sheet plane—, glowing agglomerates can be seen on the whole three-dimensional nozzle flow field. By using higher camera apertures one can reduce the out-of-plane agglomerates' signals: the higher the aperture, the smaller the depth of focus, which causes the

out-of-focal-plane agglomerates stripes to be milder. Local background filters in data pre-processing can reduce their brightness, as reported in Sect. 4.2.

In the L2K, the high-enthalpy flow is glowing itself, due to chemical reactions and high enthalpy. The glowing flow reduces the second frame's quality, due to its long acquisition time. Narrowband filters centred on laser's emission wavelength must be used.

4.2 Data analysis

Data processing was made with DaVis built-in functions. The raw images were first transformed from pixels to millimetres thanks to the calibration image taken before each experiment. They were then pre-processed to remove the background and normalize the particles' signals. As introduced in the previous section, while the first frame of the PIV image generally has good quality, the second frame suffers from the longer exposure time, capturing higher levels of noise due to the glowing flow and the glowing agglomerates. The long exposure time is physically limited by the sCMOS sensor's readout time. The high background level was reduced with DaVis built-in function "Image Preprocessing", based on local averaging, and normalization.

The PIV evaluation was performed in a selected region of the image, with rectangular shape. No major reflections caused the PIV algorithm to break, and no masking was needed. The standard DaVis built-in multi-pass PIV algorithm was used, with window shift. The initial and final Interrogation Window (IW) sizes of the multi-pass algorithm were set to $256 \times 256 \text{ px}^2$ and $64 \times 64 \text{ px}^2$, respectively, for test 1, with 50% overlap. The initial and final IW sizes were set to $512 \times 512 \text{ px}^2$ and $96 \times 96 \text{ px}^2$, respectively, for test 2, with 50% overlap (refer to Table 2 for tests characteristics). The choice of window size was based on seeding density. More resolved analysis could be performed on future tests, with a narrower light sheet and a more magnifying objective: the combination of these two actions would allow seeing smaller particles, increasing particle density.

Not all pictures of the dataset present perfect and homogeneous seeding. The vector validation process was tuned to eliminate all the vectors evaluated in the non-seeded regions of the images, deleting data computed on the noise. Non-valid vectors were strongly removed and iteratively replaced for each image.

An exemplary instantaneous PIV result of a single frame (frame n. 985, test 1, FCI) is reported in Fig. 6. The instantaneous result shows few windows where the evaluated velocity vector is non-valid—the non-valid IW is automatically discarded by the program. The velocity field is homogeneous in the core and one can clearly observe a velocity decrease in the regions corresponding to the shear layer and boundary layer of the nozzle, in the upper and lower part of the image.

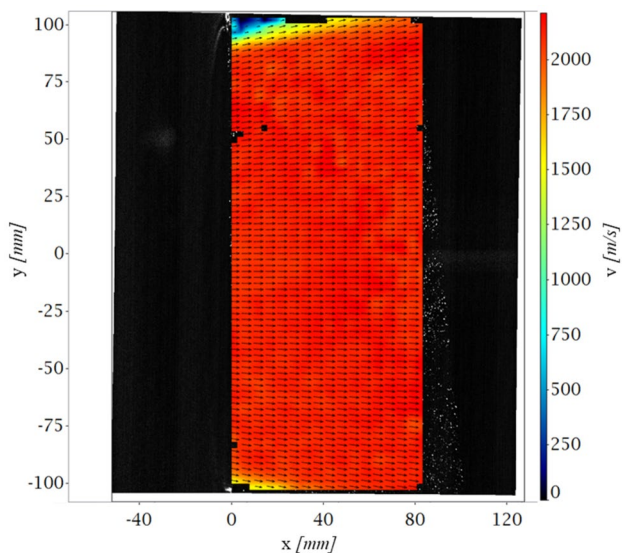


Fig. 6 Randomly selected PIV frame (number 985) from test 1, FCI

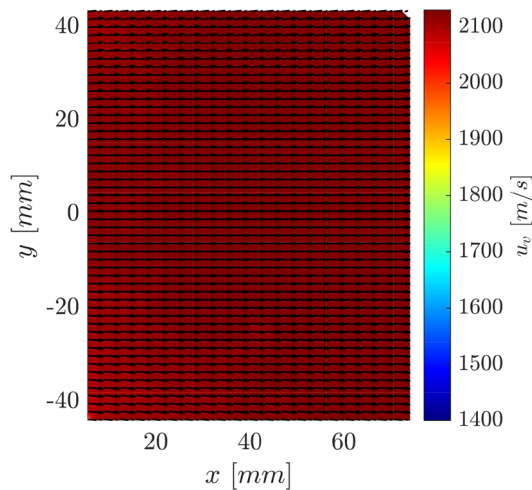


Fig. 8 Average particle velocity field, FCI, 100 mm objective (test 2, Table 2)

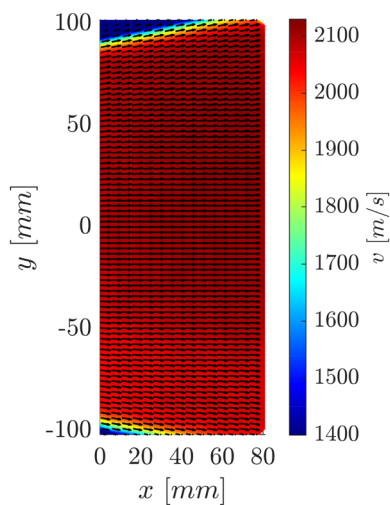


Fig. 7 Average particle velocity field, FCI, 50 mm objective (test 1, Table 2)

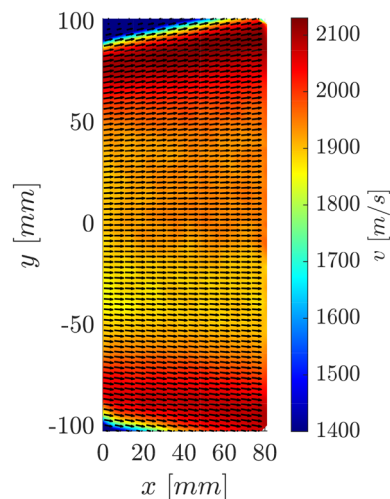


Fig. 9 Average particle velocity field, FCII, 50 mm objective (test 1, Table 2)

The final results, obtained averaging all the PIV images of one dataset, are presented in the next figures. Figures 7 and 8 are relative to FCI with two different camera objectives, namely 50 mm and 100 mm, respectively. Similarly, results for FCII are reported in Figs. 9 and 10. They are presented with horizontal vector skip of “one vector every two”, no vertical vector skip, no smoothing and linear interpolation.

Numerical Setup To compare particles velocities with the expected flow velocities, numerical simulations of the particles-free flow conditions were performed with the DLR-TAU flow solver, considering high temperature effects and non-equilibrium chemistry. A 11-species/103-reactions

chemical model was chosen for the chemical compounds CO_2 , CO , O_2 , O , NO , N_2 , N , C , C_2 , CN , NCO . Computations were performed in steady flowfield and 2D axial symmetric geometry with structured mesh. The simulations, zoomed in the relevant region of interest, are reported in Fig. 11, for both flow conditions. The Knudsen number evaluated with TAU in the whole flow core region is lower than 10^{-3} , confirming that the continuum assumption is valid.

To better appreciate the PIV results, the velocity profiles along the transversal direction (y -axis) are reported in Fig. 12. Each line of the same set corresponds to a different axial position (on the x -axis). In the figure, the PIV results are compared with the CFD simulations (for the

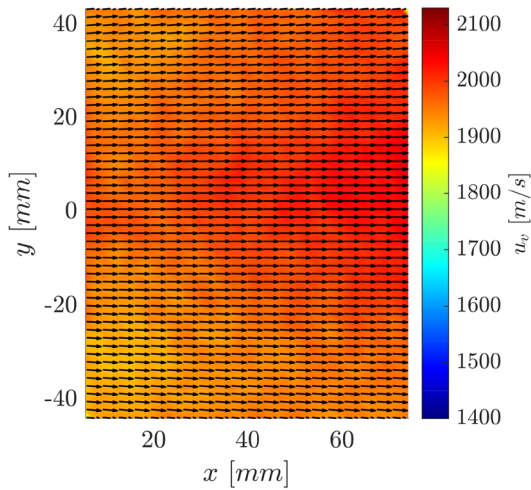


Fig. 10 Average particle velocity field, FCII, 100 mm objective (test 2, Table 2)

comparison, the CFD transversal profiles corresponding to $x = 50 \text{ mm}$ and $x = 100 \text{ mm}$ are reported). CFD flow velocities are lower for FCI than FCII, according to their different enthalpy level. The TDLAS measurements presented in Fig. 26 of Salvi et al. (2023) are reported here as errorbars, representing the statistical error of the measurements, which is lower than 5.4%. Only the measurement on the axial position of $x = 100 \text{ mm}$ is reported, for both flow conditions. The TDLAS measurement point is 20 mm downstream the right-most part of the region of interest of the PIV evaluation. The TDLAS measurement is compared with the expected CFD flow velocity on that point. The expected velocity increment between the axial positions of $x = 50 \text{ mm}$ (the position of the reported velocity profile along the transversal direction, from CFD results) and $x = 100 \text{ mm}$ is less than 0.8%, from CFD. For this reason, the TDLAS analysis is considered a valuable additional information to the PIV results, that highlights the particle velocity lag. However, the TDLAS measurements were performed without particles; in the future, the possibility of performing the same measurements in particle-laden flows should be assessed.

The velocities evaluated with PIV are considerably lower with respect to the TDLAS velocities due to the expected particles' velocity lag, in this low-density regime. Moreover, the velocity lag between particles and flow is much higher for FCII than for FCI. The two flow conditions present different qualitative and quantitative results: FCI, the one associated with lower enthalpy, has generally faster particles with respect to FCII, contrarily to what one may expect. FCII results shows that particles in the flow core are on average slower, while the outer layers carry significantly faster particles. This counter-intuitive phenomenon is not observed in FCI. In addition, in the flow core, particles of

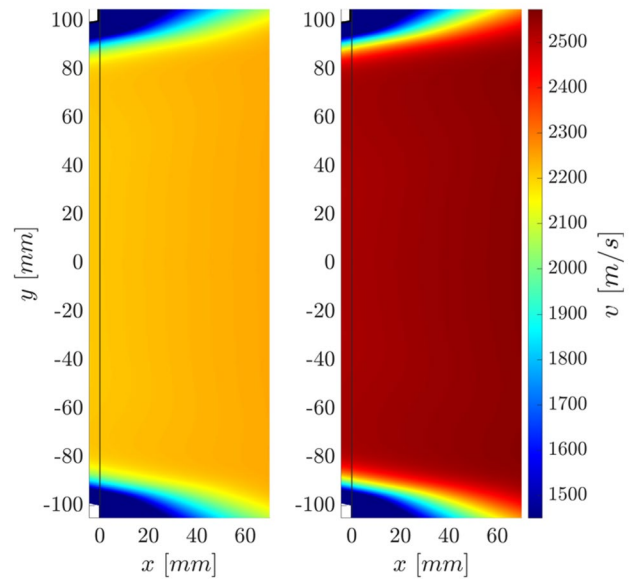


Fig. 11 Numerical simulations with DLR-TAU flow solver, FCI (left) and FCII (right). The vertical grey line represents the nozzle's exit section

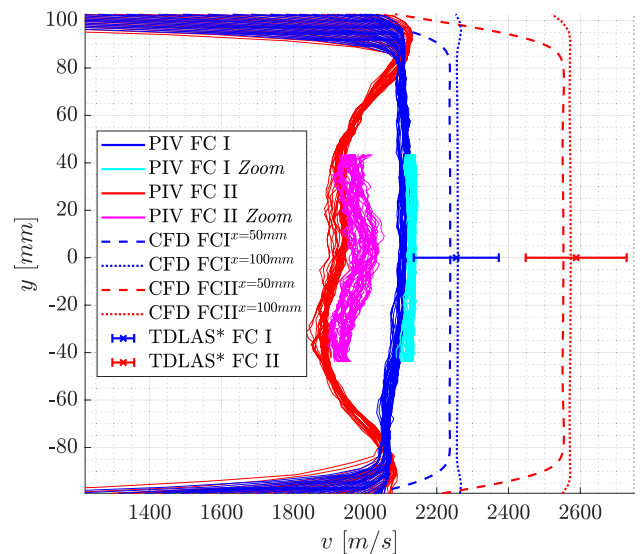


Fig. 12 Mean particles' velocity profiles along transversal direction, compared with flow velocities from CFD results (DLR-TAU flow solver) and TDLAS. CFD transversal profiles are reported only for $x = 50 \text{ mm}$ and $x = 100 \text{ mm}$ for visualization ease. In the legend, "*" refers to the axial position $x = 100 \text{ mm}$, where the TDLAS velocity measurements were performed (in Salvi et al. 2023)

FCI are faster than particles of FCII. In the outer layers, particles of FCI are slower than FCII. The velocity measured with higher zooming capabilities is slightly higher for both flow conditions. In both flow conditions one can observe that the bottom region of the flow presents averagely slower particles, suggesting that the gravitational effect could play a

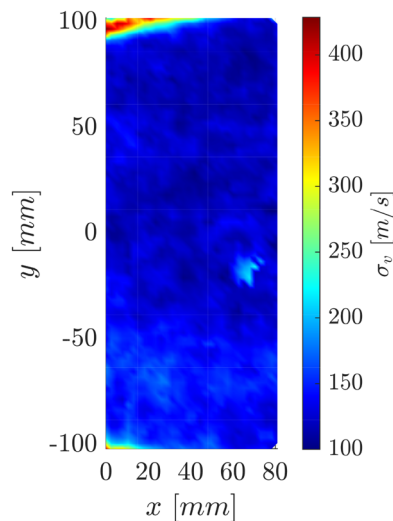


Fig. 13 Standard deviation σ_v , FCI

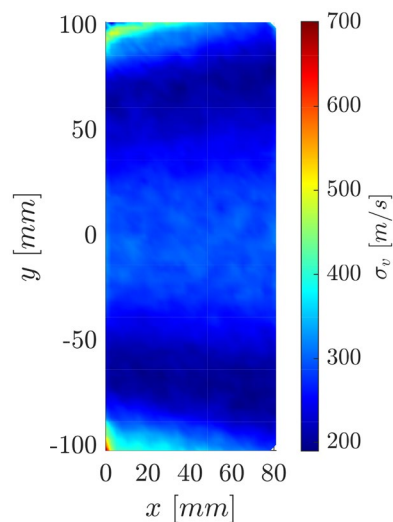


Fig. 14 Standard deviation σ_v , FCII

role in this regime: heavier—and slower—particles could be concentrated in the lower part. Both flow conditions present slower regions in correspondence with the boundary layer of the flow exiting the nozzle.

The standard deviation of velocity σ_v is reported in Figs. 13 and 14 for the two flow conditions. The uncertainty on the average velocity is evaluated by DaVis as $u_v = \sigma_v / \sqrt{N}$, where N is the number of valid vectors in the dataset, for the considered Interrogation Window. Both flow conditions have high uncertainty in the boundary layer region ($|y| > 90$ mm), and lower uncertainty in the central part of the flow ($|y| < 90$ mm). The extremal IWs in the top- and bottom-left of the evaluated region present the highest

Table 3 Relative uncertainty on the average velocity

FC	$ y < 90$ mm	Outer layers	Ext. IW*
I	$u_v < 0.4$ %	$u_v < 1$ %	$u_v < 10$ %
II	$u_v < 0.6$ %	$u_v < 2$ %	$u_v < 15$ %

*Ext. IW stands for Extremal Interrogation Windows, namely the top- and bottom-left of the results

uncertainty, as they correspond to high standard deviation and lower number of valid vectors. A summary of the uncertainty values is reported in Table 3.

For visualization ease, the profiles shown in Fig. 12 have been condensed in a single transversal profile by averaging along the x -axis. A similar procedure was performed with standard deviation profiles. In Fig. 15 the average (or condensed) velocity profiles of both FCs are reported, in comparison with the average transversal profile of standard deviation.

One can observe that the very outer regions of the flow present the highest standard deviation, in correspondence with the boundary layer exiting the nozzle. Moreover, there are other zones with high statistical variation, which differ in location between the two flow conditions. In particular, in FCII the core region presents a high standard deviation zone, while in FCI the zone with higher standard deviation lays right below the flow core. By comparing velocity and standard deviation in Fig. 15, it is observed that the regions with high standard deviation coincide with regions with averagely slower particles.

4.3 Discussion

The reasons for the counter-intuitive results, the slight asymmetries in particles velocity flow field, the faster results of the zoomed tests, and the duality between low velocity and standard deviation discussed in Sect. 4.2, are hypothesized to be due to the following possible reasons:

- Flow instability due to injection
- Spatial resolution
- Agglomeration due to melting
- Flow properties difference in different flow conditions
- Gravitational effect

These effects are discussed in the following sections.

4.3.1 Flow instability due to injection

The hypothesis of relating flow asymmetries to the particles injection process was proved to be wrong, as it was verified that the injection of the bypass flow does not change flow properties significantly: stagnation pressure and heat flux

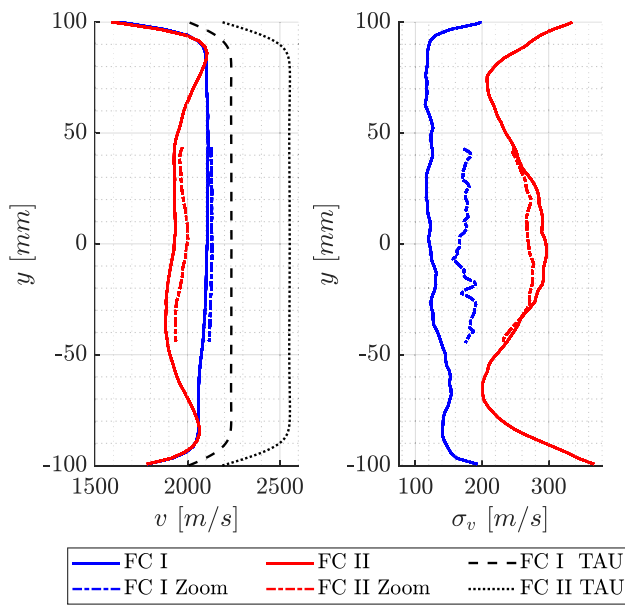


Fig. 15 Mean velocity and standard deviation profiles along the transversal direction, averaged along the x -axis

measurements were conducted, for all flow conditions, both with and without bypassing 2 g/s from the main CO₂ flow, and keeping the overall mass flow rate of CO₂ at 40 g/s, as reported in Table 1 (the bypass process is described in Sect. 3). Stagnation pressure measurement was made with a Pitot probe translating on the flow’s horizontal mid-plane, on the transversal direction, and the test result is reported in Fig. 16.² The heat flux measurement was made on flow axis with a coaxial thermocouple installed in a 25-mm-diameter cylinder oriented with its axis parallel to nozzle axis, and the result is reported in Fig. 17.

The injection of the unseeded bypass flow does not change flow thermodynamical characteristics, and it does not cause any instability or asymmetry in the flow properties. The Pitot measurements with a seeded bypass flow would be impossible, as particles would clog the probe. Heat flux measurements in the seeded flow are not trivial, and a dedicated study should be performed in the future to perform such experiment.

4.3.2 Spatial resolution

The higher level of zoom characteristic of test 2 provides higher spatial resolution, namely higher capability of picturing smaller particles. Smaller particles are thought to be faster in such conditions, thus the measured velocity is

² The higher enthalpy condition was run with 910 hPa reservoir pressure because of minor problems with the arc-heater electrodes during the test. The test is still considered valid as a proof of non-intrusivity of the bypass flow.

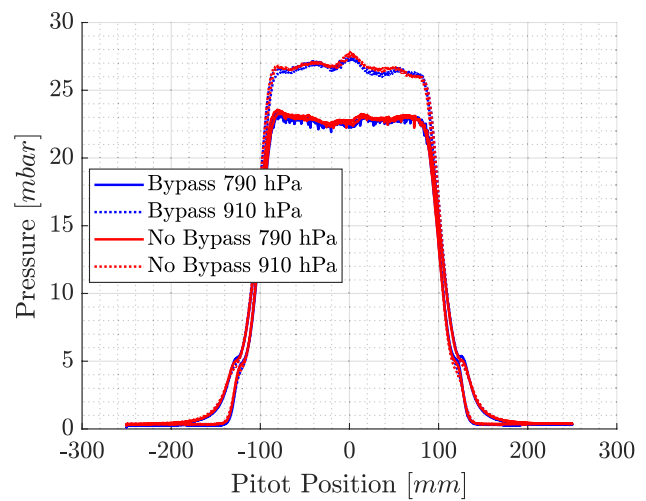


Fig. 16 Pitot measurements of FCI (continuous line) and FCII (dashed line)

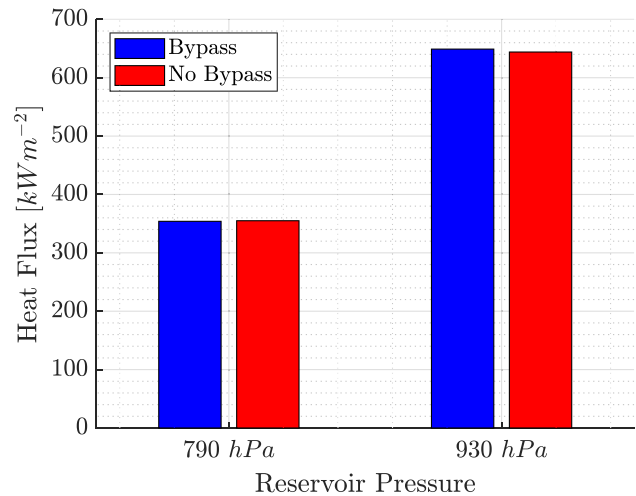


Fig. 17 Heat flux measurements

expected to be higher with higher zoom, as confirmed by experimental results. This phenomenon highlights a limit of PIV experimental technique, whose results are slightly dependent on the objective used. L2F technique could overcome this limit, at the expense of the 2-dimensionality of the result.

4.3.3 Agglomeration due to melting

One possible reason for the difference in qualitative behaviour between flow conditions could be agglomeration due to melting. MgO melting temperature ($T_m = 3125$ K, from Haynes (2011)) is, in fact, higher than the computed reservoir temperature of FCI and lower than the reservoir

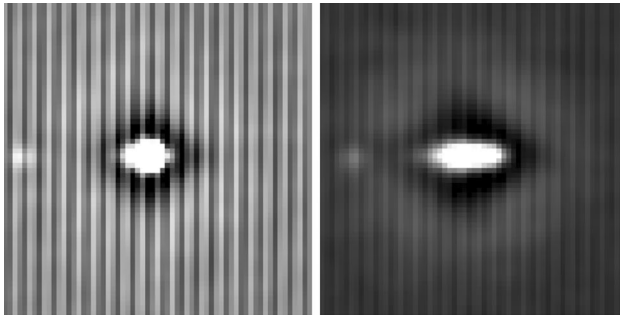


Fig. 18 Averaged correlation maps of FCI (left) and FCII (right), in position $(x, y) = (0, 40)$ mm

temperature of FCII, both reported in Table 1. For this reason, agglomeration due to melting could have more importance in FCII than in FCI, leading to the different qualitative results between the two FCs. In this sense, the number of agglomerates and heavier particles could be higher in FCII than in FCI, given the same particle size distribution as input in the reservoir. A support of this theory is the duality between the evaluated velocity and standard deviation, namely the correspondence between regions of low velocity and high standard deviation. Regions with high standard deviation coincide with regions that present a higher spread of velocities over testing time. In the same flow regions and flow conditions, one could hypothesize that bigger particles are less accelerated during the expansion along the nozzle axis due to their higher inertia. For this reason, the broad range of evaluated velocities—that correspond to a higher standard deviation—could be associated with a broad range of particle size: regions with higher standard deviation could coincide with regions where small particles and agglomerates coexist, carried by the flow with different velocities. It was observed that the averaged correlation maps of the PIV results differ between FCs: FCII presents overall more stretched correlation peaks, with respect to FCI, highlighting the broader distribution of particles velocity in the higher enthalpy flow condition, as visible in Fig. 18, where one exemplary correlation map is reported for both flow conditions, at the same position on flow axis.

The PIV algorithm is not based on particle tracking and finds only an average velocity in each interrogation window. Note that bigger particles scatter more light, they appear brighter on pictures, and tend to dominate the PIV result, which would tend to heavy particles' velocity.³ Signal normalization in pre-processing is crucial to reduce this effect. In addition, regions with broad particle velocity ranges could

³ Note that the size of a particle's image cannot be directly related to the particle's physical size due to the phenomenon of diffraction-limited imaging, reported in Raffel et al. (2018).

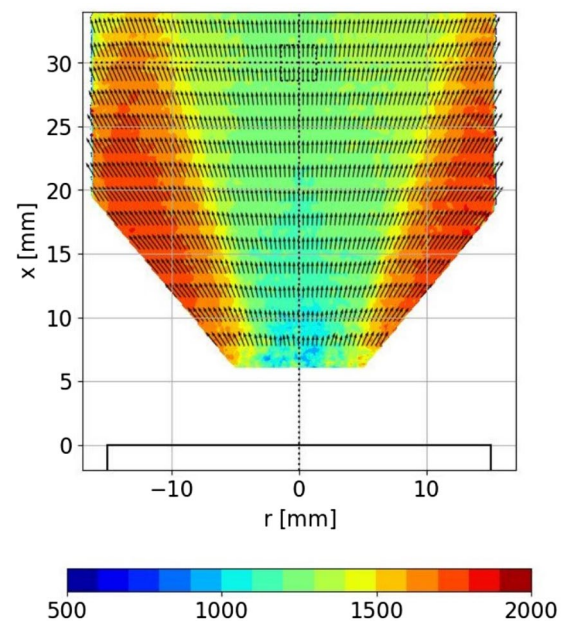


Fig. 19 EMAP. Mean velocity of test Ex1-P1. The nozzle flow is from bottom to top

be critical in determining particles velocities—if the seeding density is large enough—, considering that elastic collisions between particles moving with different velocities can happen.

In this sense, the global higher values of standard deviation in FCII results, could give a hint of the higher degree of agglomeration in the higher enthalpy flow condition.

A qualitative result similar to FCII was observed in the ESA-EMAP project (Saile et al. 2020), where PIV was used to characterize alumina particles speeds at the exit of a solid rocket motor: the outer layers of the flow carry the faster (i.e. smaller) particles, while the flow core carries the slower (i.e. bigger) particles that can't follow the flow on its outer layers, in the low-density regime of the expansion, as visible in Fig. 19. In addition, as observed in the EMAP project, the overall PIV results compute lower velocities than other techniques (e.g. laser-to-focus), as PIV evaluation is dominated by bigger particles, that have higher velocity lag.

Agglomeration due to melting effects could be verified in the future by repeating the experiments with particles with lower melting temperatures than the reservoir temperature of FCI, and observing if the qualitative result of FCI gets more similar to the one presented in Figs. 9 and 19. In addition, different tests with same particles and different reservoir temperatures (intermediate values between FCI and FCII) could be performed to better investigate how the average velocity profiles evolve when the reservoir temperature is changed.

4.3.4 Flow properties difference in different flow conditions

Another possible reason of the difference in qualitative results between the two flow conditions could be the different chemical composition of the flow, which was evaluated with CFD simulations: in such high-temperature flows, chemical reactions need to be taken into account, and different reservoir conditions lead to different chemical composition of the flow itself. The CFD simulations were validated in Salvi et al. (2023). Due to this phenomenon, the higher enthalpy flow condition (FCII) is associated to higher flow velocity—as expected—and to lower pressures, temperatures and densities, with respect to the lower enthalpy flow condition (FCI), contrarily to what one could expect. This effect is due to the different degree of dissociation of CO_2 and N_2 in the reservoir due to the different reservoir temperatures. The higher density of FCI (which is approximately double the density of FCII, as from simulations) could lead to an enhanced drag force on the particles, thus an easier particle transportation capability, and a more uniform distribution along the different flow regions, as observed in Fig. 7, contrarily to FCII (Fig. 9).

4.3.5 Gravitational effect

The slower particles' velocity evaluated in the lower region of the flow (in both FCs) could be due to the gravitational effect: heavier and bigger particles are slower, and being more subject to gravity than the smaller ones, they tend to accumulate in the bottom part of the flow. This effect is expected to be more pronounced in flow conditions with lower flow velocity: higher velocity corresponds to higher drag force on the particles, and the gravity force loses importance in favour of the drag force. For the reasons reported in Sect. 4.3.4, FCI and FCII cannot be compared in these terms, as they present a different degree of dissociation of the reservoir gas, thus a different flow density. This effect could be proved in the future by analysing different flow conditions, with different flow velocities and same flow density, and observing if the asymmetry between the lower and the upper parts of the flow is more pronounced for lower velocity conditions.

5 Conclusion

The study focused on determining particles mean velocity seeded in the free stream of the arc-heated wind tunnel L2K, with a 2D–2C particle image velocimetry (PIV) system (described in Sect. 3), in the region downstream the nozzle expansion of the wind tunnel. The results are compared with flow velocity measurements obtained with the

non-intrusive technique tunable diode laser absorption spectroscopy (TDLAS). The bypass flow used to inject particles in the main flow did not cause any flow property change, as discussed in Sect. 4.3.1.

PIV results are presented in Figs. 7, 8, 9, 10 for different flow conditions, and with different zooms given by different camera objectives. Particles speeds of more than 2000 m/s were measured. Faster results are obtained with higher zooms, as discussed in Sect. 4.3.2. One could observe the different qualitative result between the two flow conditions, which could be influenced by agglomeration of molten particles (as discussed in Sect. 4.3.3) and due to the different thermodynamical properties of the two flow conditions (as discussed in Sect. 4.3.4). Particles in the lower part of the flow are slightly slower for both flow conditions, and this effect could be due to gravity, as discussed in Sect. 4.3.5. In Fig. 12, the particles velocities evaluated with PIV are compared with CFD simulations and flow velocity measurements performed with TDLAS. The comparison between these two experimental techniques highlights the velocity lag between flow and particles.

5.1 Further improvements and outlook

This research opened the gates to high-enthalpy particle-laden flows for TPS testing, proving the feasibility of creating a testing environment that simulates the heat loads encountered during atmospheric entry on Mars, considering dust suspension in the Red Planet's atmosphere.

The most challenging aspect of this testing environment is represented by seeding a controlled amount of particles, with constant rate, being able to measure their velocities and their sizes. The high temperatures of the flow, combined with the relatively low mass flow rates, makes particles seeding very difficult to control. Further improvements on the seeding generator should aim at the realization of a dedicated device optimized for the flow conditions' mass flow rates, able to control the particles flow rates to be given as input in the wind tunnel's reservoir.

To fully characterize particle-laden flows in the L2K wind tunnel, particles size distribution should be measured in the future, and further experimental techniques should be developed or implemented in the L2K for this reason. The simplest option would be collecting the particles with an intrusive probe. The development of new techniques such as phase Doppler particle analyser (PDPA) should be investigated. In addition, particle-enhanced heat flux and erosion measurements should be developed and implemented, for the characterization of the effects of particle-laden flows on TPS. An additional experimental technique to measure particles velocity (such as L2F) could be compared to PIV results. The focus of further PIV campaigns should shift towards imaging smaller areas on flow axis, to increase the

resolution, and to obtain scientifically relevant data for stagnation heat flux measurements and erosion measurements.

The feasibility of TDLAS in particle-laden flows should be assessed, considering that this is a line-of-sight techniques, that could suffer from Signal-to-Noise Ratio reduction due to the particles. TDLAS with a translating laser line (as described in Salvi et al. 2023) could be implemented to measure the radial flow velocity profile, by applying the Abel transform. This result, combined with particles size measurements, could be valuable to validate drag models implemented in particle-laden flow solvers.

Using particle tracking techniques such as PTV could lead to a better understanding of the particles' motion and sizes: by getting more than two frames, one could get information about the particles' trajectories, and differentiate slower particles from faster particles. Another way of picturing a particle's streak would be using a laser with a longer pulse time and a camera with a comparable acquisition time. The trajectory of a particle downstream a shock could give a hint about its relative size: smaller particles tend to better follow the surrounding flow. One could exploit this effect in the future to have a further hint on particles size distribution.

Acknowledgements The authors would like to thank Prof. Isaac Boxx for his valuable scientific inputs, and the staff from the Supersonic and Hypersonic Technologies Department in DLR Köln, in particular Pascal Marquardt, Dominik Neeb, Dominik Saile, and Dirk Allofs, for their precious advice; Matthias Koslowski and Marcus Schröder for the technical support; Ansgar Marwege, Dominik Neeb and Pawel Goldyn for reviewing.

Author contributions CS contribution to this work includes methodology, design, engineering, formal analysis and investigation, original draft preparation as well as editing. AG contributed with review, funding acquisition, resources, and supervision.

Funding Open Access funding enabled and organized by Projekt DEAL. This project was funded by the DLR's Program Directorate for Space Research and Development.

Data availability There are no research data outside the submitted manuscript file.

Declarations

Conflict of interest The authors declare that they have no known competing financial interests or personal relationships that could have appeared to influence the work reported in this paper.

Consent to participate No special consent required for participation.

Consent to publish No special consent required for publication.

Open Access This article is licensed under a Creative Commons Attribution 4.0 International License, which permits use, sharing, adaptation, distribution and reproduction in any medium or format, as long as you give appropriate credit to the original author(s) and the source, provide a link to the Creative Commons licence, and indicate if changes were made. The images or other third party material in this article are included in the article's Creative Commons licence, unless indicated

otherwise in a credit line to the material. If material is not included in the article's Creative Commons licence and your intended use is not permitted by statutory regulation or exceeds the permitted use, you will need to obtain permission directly from the copyright holder. To view a copy of this licence, visit <http://creativecommons.org/licenses/by/4.0/>.

References

- Allofs D, Neeb D, Gülhan A (2022) Simultaneous determination of particle size, velocity, and mass flow in dust-laden supersonic flows. *Exp Fluids* 63:64
- ESA. ExoMars 2016 Schiaparelli Descent Sequence. <https://exploration.esa.int/web/mars/-/57465-exomars-2016-schiaparelli-descent-sequence>. Accessed: (22-07-2022)
- German aerospace center (DLR) and European space agency (ESA) (2006). Experimental and theoretical study of mars dust effects, heat transfer measurement report. Report MDUST-DLR-TN-032, Supersonic and Hypersonic Department, DLR, Köln.
- Gnemmi P, Rey C, Srulijes J, Seiler F, Haertig J (2010) Hypersonic flow-field measurements by PIV. 14th International symposium on flow visualization
- Haynes WM (2011) CRC Handbook of chemistry and physics, 92nd edn. CRC Press, Boca Raton
- Keller K, Lindenmaier P, Pfeiffer EK, Esser B, Gülhan A, Omaly P, Desjean MC (2010) Dust particle erosion during mars entry. 40th International conference on environmental systems
- Kirmse T, Agocs J, Schröder JA, Martinez Schramm, Karl S, Hanne-mann K (2011) Application of particle image velocimetry and the background-oriented schlieren technique in the high-enthalpy shock tunnel Göttingen. *Shock Waves* 21:233–241
- Lu J, Yang H, Zhang Q, Yin Zhouping (2019) PIV measurements of hypersonic laminar flow over a compression ramp. 13th International symposium on particle image velocimetry
- Neeb D, Saile D, Gülhan A (2018) Experiments on a smooth wall hypersonic boundary layer at Mach 6. *Exp Fluids* 59:68
- Palmer G, Ching E, Ihme M, Allofs D, Gülhan A (2020) Modeling heat-shield erosion due to dust particle impacts for Martian entries. *J Spacecr Rocket* 57:857–875
- Palmer G, Sahai A, Allofs D, Gülhan A (2022) Comparing particle flow regimes in the L2K Arcjet with Martian entry conditions. FAR
- Raffel M, Willert CE, Scarano F, Kähler CJ, Wereley ST, Kompenhans J (2018) Particle image velocimetry—a practical guide, 3rd edn. Springer International Publishing AG, Cham, Switzerland
- Saile D, Allofs D, Kühl V, Riehmer J, Steffens L, Gülhan A, (DLR AS-HYP), Beversdorff M, Förster W, Willert Ch (DLR AT-OTM), Carlotti S, Maggi F (SPLab, Polimi), Liljedahl M, Wingborg N (FOI) (2020) Experimental modeling of alumina particulate in solid booster: final report. Report ESA contract no. 4000114698/15/NL/SFe, German Aerospace Center (DLR), Department of Supersonic and Hypersonic Technologies, Köln, DE
- Salvi C, Steffens L, Hohn O, Gülhan A, Maggi F (2023) Martian flow characterization using tunable diode laser absorption spectroscopy, in high enthalpy facilities. *Acta Astronaut* 213:204–214
- Schrijer FFJ, Scarano F, van Oudheusden BW (2006) Application of PIV in a Mach 7 double-ramp flow. *Exp Fluids* 41:353–363
- Sub Lee G, Sakkos P, Gessman I, Lim J, Kato N, Kirchner BM, Elliott G, Lee T (2022) PIV Measurements and total temperature thermometry of a Mach 4.5 Arc-heated Nozzle Flow. *AIAA 2022-2337*

Publisher's Note Springer Nature remains neutral with regard to jurisdictional claims in published maps and institutional affiliations.